Topology of Gel-Phase Domains and Lipid Mixing Properties in Phase-Separated Two-Component Phosphatidylcholine Bilayers

Vincent Schram, Hai-Nan Lin, and Thomas E. Thompson
Department of Biochemistry, University of Virginia, Charlottesville, Virginia 22908 USA

ABSTRACT The influence of the lipid mixing properties on the lateral organization in a two-component, two-phase phosphatidylcholine bilayer was investigated using both an experimental (fluorescence recovery after photobleaching (FRAP)) and a simulated (Monte Carlo) approach. With the FRAP technique, we have examined binary mixtures of 1-stearoyl-2-capryl-phosphatidylcholine/1,2-distearoyl-phosphatidylcholine (C18C10PC/DSPC), and 1-stearoyl-2-capryl-phosphatidylcholine/1,2-dipalmitoyl-phosphatidylcholine (C18C10PC/DPPC). Comparison with the 1,2-dimyristoyl-phosphatidylcholine/1,2-distearoyl-phosphatidylcholine (DMPC/DSPC) previously investigated by FRAP by Vaz and co-workers (*Biophys. J.*, 1989, 56:869–876) shows that the gel phase domains become more effective in restricting the diffusion coefficient when the ideality of the mixture increases (i.e., in the order C18C10PC/DSPC → C18C10PC/DPPC → DMPC/DSPC). However, an increased lipid miscibility is accompanied by an increasing compositional dependence: the higher the proportion of the high-temperature melting component, the less efficient the gel phase is in compartmentalizing the diffusion plane, a trend that is best accounted for by a variation of the gel phase domain shape rather than size. Computer-simulated fluorescence recoveries obtained in a matrix obstructed with obstacle aggregates of various fractal dimension demonstrate that: 1) for a given obstacle size and area fraction, the relative diffusion coefficient increases linearly with the obstacle fractal dimension and 2) aggregates with a lower fractal dimension are more efficient in compartmentalizing the diffusion plane. Comparison of the simulated with the experimental mobile fractions strongly suggests that the fractal dimension of the gel phase domains increases with the proportion of high-temperature melting component in DMPC/DSPC and (slightly) in C18C10PC/DPPC.

INTRODUCTION

Although it is now well demonstrated that in-plane domains exist in the plasma membrane of eukaryotic cells (Tocanne, 1992), their detailed organization is still an open problem. In addition to lateral protein-protein organization and interaction of membrane components with the cytoskeleton (Sheetz et al., 1980), the lateral phase separation of lipid molecules may play an important role in membrane microdomain formation and organization. Even though no distinct phase transitions can be observed by calorimetry in plasma membranes (Wolf et al., 1990), presumably because of the great diversity of lipid species and to the presence of high concentrations of cholesterol, the existence of biomembrane domains with different lipid fluidity cannot be ruled out a priori.

Over the past few years, the lateral organization adopted by a two-component lipid membrane in the liquid crystalline/gel phase coexistence region has been investigated in a variety of phosphatidylcholine mixtures using the fluorescence recovery after photobleaching (FRAP) technique (Vaz et al., 1989, 1990; Bultmann et al., 1991, Almeida et al., 1992). Because the translational diffusion coefficient in the gel phase is much lower than in the fluid phase (estimated to be 1/10th to 1/1000th), the FRAP data (diffusion coefficient, D, and mobile fraction, M) have been interpreted in terms of two-dimensional percolation of the fluid phase (Stauffer and Aharony, 1992), with the gel phase treated as a nonconducting phase: a mobile fraction less than 1 is analyzed as a compartmentalization of the diffusion plane, i.e., as the formation of closed cavities in which the diffusion is restrained. Thus, the higher the area fraction of gel phase at which M drops, and the more centrosymmetric (or less ramified) are the gel phase domains (Vaz et al., 1989 and 1990, Bultmann et al., 1991).

Beyond these qualitative ramified or centrosymmetric designations derived from M data, the domain sizes can be estimated from the decrease of the diffusion coefficient due to the obstruction effect of the gel phase domains by using the results of Monte Carlo simulations (Eisinger et al., 1986; Saxton, 1989, 1992; Schram et al., 1994) or analytical treatments (Almeida et al., 1992, Barros et al., 1992). These approaches show that, for nonoverlapping immobile obstacles of a given size and shape, the normalized diffusion coefficient D^* decreases almost linearly as the obstacle area fraction increases. A linear decrease of experimental D^* versus the gel phase area fraction is thus a good indication

Received for publication 12 March 1996 and in final form 20 June 1996.

Abbreviations used: c, area fraction of obstacles to diffusion; C18C10PC. 1-stearoyl-2-capryl-phosphatidylcholine; D, lateral diffusion coefficient; D^*, normalized diffusion coefficient; Df, fractal dimension; DMPC, 1,2-dimyristoyl-phosphatidylcholine; DPPC, 1,2-dipalmitoyl-phosphatidylcholine; DSPC, 1,2-distearoyl-phosphatidylcholine; FRAP, fluorescence recovery after photobleaching; l.s., lattice spacing; M, mobile fraction; NBD-C18C10PE, *N*-(7-nitrobenzoxa-2,3-diazol-4-yl)-1-stearoyl-2-capryl-phosphatidyl-ethanolamine; NBD-DLPE, *N*-(7-nitrobenzoxa-2,3-diazol-4-yl)-dilauroyl-phosphatidylethanolamine; NBD-DPPE, *N*-(7-nitrobenzoxa-2,3-diazol-4-yl)-dipalmitoyl-phosphatidylethanolamine; NBD-DOPE, *N*-(7-nitrobenzoxa-2,3-diazol-4-yl)-dioleoyl-phosphatidylethanolamine; P_{agg}, probability of aggregation of point obstacles; ESR, electron spin resonance.

Address reprint requests to Dr. Thomas E. Thompson, Department of Biochemistry, University of Virginia, School of Medicine, Box 440, Charlottesville, VA 22908. Tel.: 804-924-2651; Fax: 804-924-5069; E-mail: tet@virginia.edu.

0006-3495/96/10/1811/12 $2.00

that the topology of the gel phase domains remains constant all across the phase diagram. Even though this point was demonstrated for highly immiscible lipid mixtures such as DPPC/*N*-lignoceroyldihydro-galactosylceramide (Almeida et al., 1992), it may not be true with lipids that mix more ideally.

Indeed, an ESR study (Sankaram et al., 1992) together with a recent fluorescence quenching investigation (Piknova et al., 1996) clearly suggest that even in the peritectic mixture 1,2-dimyristoyl-phosphatidylcholine/1,2-distearoyl-phosphatidylcholine (DMPC/DSPC), the average sizes of the fluid and gel phase domains vary across the phase diagram. These data favor a model of liquid crystalline → gel phase transition proceeding by the growth of a constant number of gel phase domains, instead of an increase in the number of domains. Lipid components mixing well together, with a low compositional difference and a low energetic difference between the coexisting fluid and gel phases are likely to form in the two-phase coexistence region gel phase domains of small size and/or of ramified structure. However, a highly immiscible lipid mixture, with a higher compositional difference and a higher energetic difference between the coexisting fluid and gel phases will probably organize in larger and/or more centrosymmetric gel phase domains. Although proposed as a key factor regulating the shape and time stability of the gel phase domains (Vaz, 1992), the influence of the lipid mixing properties on the membrane lateral organization has not been investigated thus far.

Because the topology of the gel phase domains seems to vary across the phase diagram in the DMPC/DSPC mixture, lipid systems of higher immiscibility are expected to display less compositional dependence. Although mixtures including either dilauroyl-phosphatidylcholine or diarachidonyl-phosphatidylcholine represent a priori the simplest choice, their bilayer thickness difference at the gel/fluid interface would be much larger than in DMPC/DSPC, which is likely to bias a comparison of the gel phase domain topology: computer simulations using a molecular interaction model clearly suggest that an increasing bilayer thickness gap at the gel/fluid interface, subsequent to a larger acyl chain length difference of the lipid components, leads to the formation of large centrosymmetric domains (Jorgensen et al., 1993). Moreover, a similar approach shows that a layer of gel-phase molecules of the low-temperature melting component may accumulate at the fluid/gel boundary (Jorgensen and Mouritsen, 1995), which may account for the necessity to consider the presence of an annulus of motionally restricted lipids around each gel phase domain to obtain a realistic value of their size (Almeida et al., 1992).

Lowering the miscibility without increasing the mismatch at the gel/fluid interface is thus critical and can be achieved by substituting for DMPC the asymmetric acyl-chain phosphatidylcholine of identical molecular weight, 1-stearoyl-2-capryl-phosphatidylcholine (C18C10PC). C18C10PC adopts in the gel phase a mixed-interdigitated configuration in which the longer acyl chain spans the entire bilayer, resulting in three acyl chain cross-sectional areas per headgroup (McIntosh et al., 1984; Slater and Huang, 1988). Above its phase transition temperature, C18C10PC exhibits partial dynamic interdigitation (Halladay et al., 1990; Mason, 1994), but with no measurable effect on the long-range translational diffusion coefficient measured by FRAP (Schram and Thompson, 1995). Moreover, the bilayer thickness of liquid crystalline C18C10PC is almost identical to fluid DMPC (Hui et al., 1984). Thus, one can reasonably consider that in lipid mixtures whose low-temperature melting component is either DMPC or C18C10PC and high-temperature melting component is either DPPC or DSPC, the bilayer thickness difference at the gel/fluid interface does not vary much.

In the present study, we have investigated by FRAP the translational diffusion of NBD-PE probes in C18C10PC/DPPC and C18C10PC/DSPC mixtures as a function of temperature. C18C10PC/DSPC, a highly immiscible lipid mixture, was investigated by Mason (1988), and we have established the phase diagram of C18C10PC/DPPC by differential scanning calorimetry. These two lipids display a limiting case of an eutectic mixture, with the eutectic point too close to pure C18C10PC to be detected. An unusual feature of the phase diagram of this system is the presence of an inflection point on the liquidus line between 20 and 40% of DPPC, probably associated with a continuous transition of the liquid crystalline phase from a dynamic partially interdigitated to a "classical" (i.e., noninterdigitated) conformation.

Plots of the normalized diffusion coefficient D^* versus the gel phase area fraction obtained in the three lipid mixtures show an increasing efficiency of the gel phase domains to restrict the diffusion coefficient when the ideality of the mixture increases (in the order C18C10PC/DSPC → C18C10PC/DPPC → DMPC/DSPC). This trend strongly suggests a reorganization of the gel phase domains in smaller and/or more ramified structures in more nearly ideal lipid mixtures, as can be expected. Size and fractality may be discriminated by the mobile fraction values, as a reduction of the fractal dimension of the gel phase domains should have a major effect on the efficiency to compartmentalize the diffusion plane, i.e., in restricting M. Unfortunately, the mobile fractions display a compositional dependence which increases with the ideality of the mixture, thus complicating this analysis: in a given mixture, the higher the proportion of the high-temperature melting component, the less efficient is the gel phase in obstructing the long-range translational diffusion. This trend, absent in C18C10PC/DSPC, clear in C18C10PC/DPPC, and considerable in DMPC/DSPC, is most likely due to an increase of the fractal dimension of the gel phase domains at high ratio of high-temperature melting lipid.

To clarify the impact of the obstacle fractality on the diffusion coefficient and mobile fraction measured by FRAP, we have developed simple computer simulations of fluorescence recovery curves in a matrix obstructed with aggregates of point obstacles. These clusters are generated by a self-obstructed diffusion process of point obstacles,

which irreversibly stick with a defined probability when they come in contact with a nucleation site or with a point obstacle already in contact with one. An aggregation probability of 1 yields highly ramified aggregates, with a low fractal dimension and a high efficiency in restricting diffusion, whereas lower probabilities of aggregation lead to more compact aggregates, whose fractal dimension grows toward 2 and are less efficient in obstructing the diffusion. This model was chosen by us as a simple way to generate essentially centrosymmetric structures with variable interface detail. We do not intend to imply that there is any physical basis for believing the solid domains in the bilayer form by this process or have this shape in detail. Certainly the aggregation probability has no link to the mixing properties of the lipid components.

For a constant average aggregate size, we found a linear increase of the relative diffusion coefficient with the fractal dimension of the aggregates. This linear relationship, valid only in an essentially open diffusion plane (M close to 1), should not depend of the radius of observation and thus may be applied to experimental FRAP measurements. The obstacle fractality has also a major impact on the mobile fraction: highly ramified aggregates are extremely efficient in compartmentalizing the diffusion plane, whereas a higher area fraction of compact aggregates is required to form closed cavities. The variation of M with a decreasing probability of aggregation closely resembles the compositional dependence evidenced on the mobile fractions mainly by DMPC/DSPC and, to a lesser extent, by C18C10PC/DPPC. This observation further support the view that the fractal dimension of the gel phase domains increases with the proportion of high temperature melting component in DMPC/DSPC and (slightly) in C18C10PC/DPPC.

Even though the data obtained on the highly immiscible lipid mixture C18C10PC/DSPC can be analyzed with a classical model of nonoverlapping circular obstacles (Schram et al., 1994) to yield a gel phase domain size of ~500 lipid molecules, the interplay of the obstacle size and fractality, which may compensate each other, renders difficult a deeper analysis of the FRAP data obtained on C18C10PC/DPPC and DMPC/DSPC. However, these results, together with the variation of size evidenced in DMPC/DSPC by other approaches (Piknova et al., 1996; Sankaram et al., 1992), clearly suggest that an increasing miscibility of the lipid components complicates the topology adopted by the gel phase domains, in terms of size, fractality, and compositional dependence.

MATERIALS AND METHODS

Chemicals

C18C10PC, DPPC, DSPC, NBD-DPPE, and NBD-DOPE were purchased from Avanti Polar Lipids (Eugene, OR). All other chemicals were of analytical grade.

Calorimetry

Separate chloroform solutions of C18C10PC and DPPC were mixed, and the solvent was removed in a rotary evaporator at 55°C. The samples were then dissolved in benzene, colyophilized, and kept overnight under high vacuum. The lipid mixtures were hydrated with a buffer NaCl 10 mM, NaH_2PO_4 5 mM, EDTA 1 mM pH = 7.42, heated 15 min at 55°C, and cooled down to room temperature three times. Samples were incubated 3 h at 4°C before differential scanning calorimetry scans performed at a heating rate of 15°C/h on a Microcal MC-2 differential calorimeter (Microcal, Inc., Amherst, MA). Two or three differential scanning calorimetry runs were performed for each lipid composition and averaged. The onset and completion temperatures were determined with the software supplied by Microcal.

Multibilayers

Supported multibilayers were formed following the standard protocol of Vaz et al. (1985), with a molar ratio phosphatidylcholine/fluorescent probe of 2/1000. The standard buffer was NaCl 10 mM, Na_2HPO_4 5 mM, NaH_2PO_4 5 mM, EDTA 10^{-5} M, pH = 7. The samples were incubated 2 days at 10°C above their phase transition temperature before measurement.

FRAP experiments

FRAP experiments were carried out on an ACAS 470 workstation (Meridian Instruments, Okemos, MI). In this apparatus, the 488-nm line of an argon ion laser (Coherent 90 SUV) operated at 200 mW is split by an acoustic-optic modulator. The resultant first order beam is used as a bleaching (100% power) or monitoring (<10% power) beam in an inverted microscope equipped with a 40× air objective and a motorized stage. After the photobleaching phase, the fluorescence intensity profile is scanned repeatedly through the bleaching area by computer driven translations of the microscope stage. The laser power supply, acoustic optic modulator, and motorized stage are interfaced with an IBM compatible microcomputer and operated by the software provided by Meridian. Note that between two consecutive scans (typically 90% of the time), the beam is "parked" far away from the observation area and thus does not bleach the sample as it would with steady illumination.

Recovery scans were analyzed with the diffusion function of Koppel (1979). The diffusion coefficient D, the mobile fraction M, and three parameters of the shape of the initial Gaussian profile of the fluorophore concentration (maximum bleaching amplitude, $\alpha 0$; half-width at half-high, $\omega 0$; and x-coordinate of $\alpha 0$) were adjusted to obtain the best fit between the experimental points and the diffusional function. Each D and M value reported is the average of 40 recoveries recorded on four different samples. The standard deviations are always less than ±15% on D, ±3% on M.

The temperature of the sample was regulated by a Peltier stage unit. Multilayers were preincubated at the highest temperature of the scan for 1 h, then cooled down in steps of 3°C, allowing 30 min of equilibration at each temperature before measurement.

Simulation of fluorescence recovery curves

A portion of a flat membrane was modeled by a square area of a 500 × 578 sites triangular lattice with periodic boundary conditions. Each site of the lattice can be either empty, occupied by an obstacle or a tracer. The equivalent of the spot FRAP fluorescence intensity is determined by counting the number of tracers present in a circular observation area of 50 lattice spacings (l.s.) radius in the center of the lattice. All the lattice sites are examined sequentially, a scan of the whole matrix represents a time step of the system. When a site bears a tracer, a direction of jump is chosen at random among the six possible. Unless the destination site is occupied by an obstacle, the tracer jumps to the neighboring site, even if the destination site is already occupied by another tracer. The situation in which several tracers occupy the same position has no physical relevance

but is intended to simulate a purely random diffusion process and avoid self-obstruction diffusion effects, which increase rapidly with the tracer area fraction (Abney et al., 1989). With an equilibrium perturbation such as a FRAP experiment, tracer-tracer obstruction would give rise immediately after the bleaching to the equivalent of a chemical potential between the observation area (tracer-depleted) and the surrounding medium, thus biasing the recovery.

Fluorescence recovery curves are generated in three steps:

1) A total of 10% of the matrix sites, chosen at random, is initially occupied by tracers, and the system is equilibrated on a 1000 time steps run. I_o, the prebleach fluorescence intensity, is set equal to the average number of tracers present in the observation area during this equilibration phase.

2) The photobleaching process is then simulated by erasing all the tracers present in the observation area.

3) The fluorescence intensity is recorded over 15,000 time-steps. A complete recovery mobilizes ~1000 tracers, a number high enough to ensure a good signal/noise ratio for each recovery curve. The resolution is further improved by recording several recoveries and averaging them, allowing eventual obstacles distribution heterogeneities in and around the observation area to be averaged. The resultant recovery curve is analyzed with the standard spot-FRAP diffusional functions (Lopez et al., 1988) with the bleached area radius equal to 50 l.s. The agreement between the simulated recoveries and the best-fit diffusional curves is excellent with the standard deviation between them $<10^{-2}$ in every case. In an obstacle-free lattice, we obtained, by averaging 10 recoveries, a diffusion coefficient of 0.241 arbitrary unit and a mobile fraction of 0.998, with a standard deviation of 0.0054. D values are normalized relative to this obstacle-free reference to give a relative diffusion coefficient, D^*.

The obstacles, either points or aggregates, are distributed before introducing the tracers, with a new distribution for each recovery recorded. Aggregated obstacles are generated with a diffusion limited aggregation process derived from the model developed by Saxton (1992): a fraction of the point obstacles (1 in 250) is assigned as immobile nucleation sites. The system then undergoes an aggregation phase, in which the mobile point obstacles diffuse randomly. The aggregation is modeled as a self-obstructed process, i.e., when a point obstacle tries to jump to a site occupied by another point obstacle, the jump fails. When a point obstacle comes in contact with a nucleation site, it sticks irreversibly to it and becomes part of a growing nucleation cluster if a random number chosen between 0 and 1 is larger than an initially assigned probability of aggregation, P_{agg}. When a point obstacle comes in contact with several nucleation sites, an equal number of attempts are made to aggregate. Obstacle aggregates are not allowed to diffuse. The aggregation goes on until all point obstacles become part of some nucleation cluster.

In such a model, the density of the nucleation sites determines the scale length at which the aggregation takes place (average aggregate size), whereas the probability of aggregation determines the fractality (ramified or compact shape) of the aggregates (Saxton, 1992). For each obstacle area fraction and probability of aggregation, the fractal dimension Df of the aggregates is calculated from the slope of the cluster weights (number of lattice sites) versus their radius of gyration in a double-logarithmic plot (Stauffer and Aharony, 1992). Note that because of cluster merging, the average cluster size becomes significantly larger than 250 lattice sites above an obstacle area fraction of 20% (Table 1). For that reason, Df is calculated only from clusters whose weight does not exceed 250 sites. The fractal dimensions in Table 1 thus reflect the cluster topology resulting from the aggregation process, not cluster merging. Both become significantly different at high obstacle area fractions and low probability of aggregation. We also determined the lowest obstacle area fraction at which the matrix contains at least one cluster of weight larger than 32,000 lattice sites, that is of a scale-length comparable to the matrix dimensions. Although that point does not represent exactly the percolation threshold, it gives an estimate of it in the 10% obstacle area fraction increment we used.

To compensate for obstacle distribution heterogeneities, due either to a low number of aggregate or to a large aggregate size (see Table 1), we averaged 10 recoveries for aggregates at 10 and 20% area fraction for all probabilities of aggregation and above 30% obstacle area fraction for probability of aggregation of 1/100 and 1/1000. For all other conditions, five recoveries were averaged.

RESULTS

Phase diagram of C18C10PC/DPPC

As the phase diagram of C18C10PC/DPPC has not previously been determined, we have examined mixtures of these two phosphatidylcholines by differential scanning calorimetry. The heat capacity curves as a function of temperature for different mole fractions of C18C10PC in DPPC are plotted in Fig. 1. The sharp endotherm of pure C18C10PC centered at 17.4°C broadens appreciably when the DPPC content increases from 0 to 20%. At more than 20 mol % DPPC, the heat capacity curves display broad, high temperature wings, but the onset temperature remains constant at 17.4°C up to 70% of DPPC. Between 20 and 40% DPPC, the completion temperature increases markedly from 22.5 to 34.8°C, then slowly goes up to 41.4°C above 40% DPPC. At 50% DPPC, a clear high temperature endotherm begins to appear, shifting to higher temperatures when the DPPC content increases, before finally merging with the pure DPPC endotherm. Above 70% DPPC, the low temperature endotherm wing merges with the high temperature one.

The onset and completion temperatures determined from these thermograms were used to construct the phase diagram of the C18C10PC/DPPC mixture (Fig. 2B). The invariance of the onset temperature at 17.4°C, corresponding to the phase transition temperature of pure C18C10PC, indicates that a gel phase, G1, of almost pure C18C10PC coexists with a DPPC-rich gel phase, G2. This extended gel phase immiscibility is not unexpected because C18C10PC adopts a mixed-interdigitated conformation in the gel phase, in which the bilayer thickness is considerably smaller than the noninterdigitated gel DPPC (McIntosh et al., 1984). In the same way, the solubility of fluid phase DPPC in the mixed interdigitated gel phase C18C10PC is extremely low, probably due to the important difference in bilayer thickness between both phases. C18C10PC/DPPC is thus likely to be a limiting case of an eutectic mixture, with the eutectic point too close to pure C18C10PC to be detected.

The unusual shape of the liquidus line with an inflection point (Fig. 2 *B*) may be accounted for by the peculiar nature of the liquid crystalline phase of C18C10PC. At <20% DPPC, it must present the same kind of dynamic partial interdigitation as pure fluid C18C10PC (Halladay et al., 1990; Mason, 1994). The inflection zone, between 20 and 40% DPPC, is likely to correspond to a continuous transition of the fluid phase from a dynamic partially interdigitated to a classical (i.e., noninterdigitated) configuration.

The phase diagram of the C18C10PC/DSPC mixture, established by Mason (1988) is shown in Fig. 2 *A*. These two lipids are highly immiscible in the gel phase, and even display a limited region of liquid-liquid immiscibility, F1+F2. The main gel/liquid crystalline phase coexistence region, F1+G3, consists of a DSPC-rich (>95%) gel phase coexisting with a C18C10PC-rich (>80%) fluid phase (Fig. 2 *A*) (see Mason, 1988). The phase diagram of DMPC/

TABLE 1 Computer simulated recovery curves: variation of the diffusional parameters *D and *M* and of the aggregate topology (fractal dimension *Df*, average weight, and average radius of gyration Rgyr, with SD) with the obstacle area fraction c and the probability of aggregation P_{agg}. *p* = percolating aggregate. *Df* and Rgyr are calculated only below the obstacle percolation threshold**

c	*D**	*M*	*Df*	Weight ± SD	Rgyr ± SD
0	1.00	1.00			
Random points					
0.1	0.89	0.96			
0.2	0.70	0.94			
0.3	0.47	0.95			
0.4	0.21	0.90			
0.5	1.07	0.23			
0.6	35.48	0.05			
0.7	481.33	0.03			
Aggregates P_{agg} = 1					
0.1	0.59	0.91	1.45	250 ± 131	12.7 ± 4.0
0.2	0.40	0.78	1.53	254 ± 154	12.0 ± 4.3
0.3	0.64	0.50	1.61	305 ± 260	11.8 ± 5.7
0.4	1.00	0.26	*p*	*p*	*p*
0.5	8.13	0.09	*p*	*p*	*p*
0.6	180.50	0.04	*p*	*p*	*p*
Aggregates P_{agg} = 1/10					
0.1	0.69	0.93	1.51	251 ± 127	11.8 ± 3.6
0.2	0.46	0.86	1.54	258 ± 140	10.6 ± 3.4
0.3	0.40	0.77	1.53	276 ± 152	9.8 ± 3.0
0.4	0.42	0.67	1.63	372 ± 267	10.4 ± 4.1
0.5	0.74	0.39	1.68	912 ± 1511	14.7 ± 10.9
0.6	1.29	0.22	*p*	*p*	*p*
0.7	15.31	0.08	*p*	*p*	*p*
Aggregates P_{agg} = 1/100					
0.1	0.76	0.94	1.57	252 ± 120	9.2 ± 2.6
0.2	0.60	0.95	1.64	266 ± 130	8.0 ± 2.2
0.3	0.55	0.94	1.69	307 ± 151	7.9 ± 2.2
0.4	0.55	0.88	1.69	375 ± 211	8.4 ± 2.7
0.5	0.57	0.82	1.80	590 ± 458	10.5 ± 4.9
0.6	0.50	0.67	1.77	1384 ± 1795	16.2 ± 12.1
0.7	1.10	0.41	*p*	*p*	*p*
Aggregates P_{agg} = 1/1000					
0.1	0.80	1.00	1.77	264 ± 109	6.9 ± 1.5
0.2	0.83	0.95	1.85	323 ± 161	7.3 ± 2.1
0.3	0.93	0.89	1.84	434 ± 260	8.5 ± 3.1
0.4	0.83	0.89	1.86	691 ± 653	10.9 ± 6.3
0.5	0.84	0.73	1.89	1385 ± 2099	15.3 ± 13.0
0.6	1.26	0.60	*p*	*p*	*p*
0.7	1.68	0.42	*p*	*p*	*p*

DSPC, refined by Knoll et al. (1991) by small-angle neutrons scattering, is shown in Fig. 2 *C*.

We will adopt the point of view that the ideality of a lipid mixture can be approximated by the deviation of the fluidus and solidus lines from the straight line connecting the transition temperatures of both lipids, relative to their difference in transition temperature. The progression from C18C10PC/DSPC (Fig. 2 *A*) to C18C10PC/DPPC (Fig. 2 *B*) to DMPC/DSPC (Fig. 2 *C*) thus corresponds to an increase of the mixture ideality, even though it does not strictly parallel the temperature extent of the two-phase coexistence region.

FRAP experiments

We used NBD-DOPE as fluorescent probe for the lipid mixture C18C10PC/DSPC and NBD-DPPE for the lipid mixture C18C10PC/DPPC. Although the lateral diffusion coefficient has not been reported to depend on the acyl chains of the probe or of the host lipid (Vaz et al., 1984), a fluorescent probe with acyl chains much shorter than the high-temperature melting lipid may accumulate at the gel/fluid interface (Jorgensen et al., 1993), and thus not report accurately the diffusion in the liquid crystalline phase. Moreover, to remain consistent with most published simulations and analytical treatments of obstructed diffusion, we performed only cooling scans, thus promoting the formation of gel phase domains in a continuous liquid crystalline phase.

The diffusion coefficients obtained in C18C10PC/DSPC and C18C10PC/DPPC are shown as Arrhenius plots in Fig. 3, *A* and *B*. We compare our data with those obtained with NBD-DLPE in DMPC/DSPC by Vaz et al. (1989) (cooling

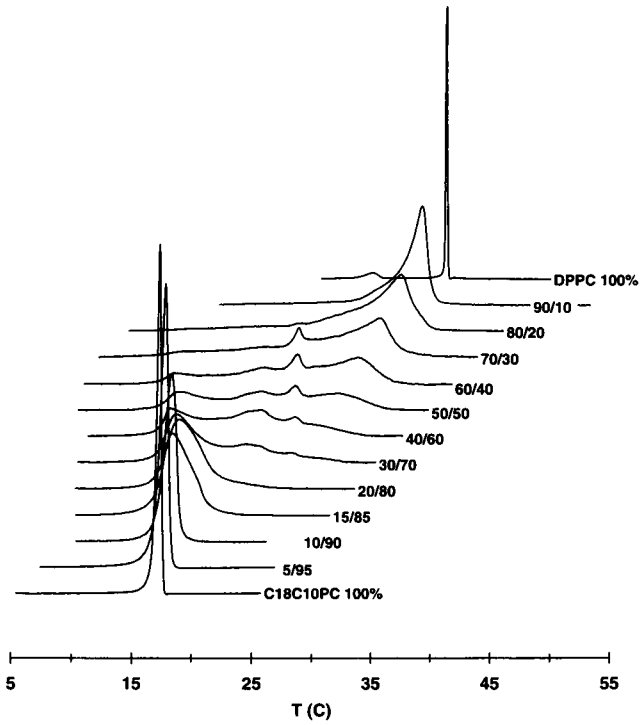

FIGURE 1 Differential scanning calorimetry heating thermograms for samples of DPPC containing various amounts of C18C10PC. The heat capacity curves of the pure components have been reduced to fit on the plot.

scans) in Fig. 3 *C*. In this case, the diffusion coefficients for the homogeneous fluid phase were calculated from the D values at temperatures above the fluidus line in DMPC/DSPC mixtures (Vaz et al., 1989). On an Arrhenius plot, these points are well fitted by a straight line (data not shown), yielding an activation energy of 6.9 kcal/mol, well within the range commonly found for the lateral diffusion of a phospholipid analog in a liquid crystalline phase bilayer (Almeida et al., 1992; Vaz et al., 1985).

As expected at a given temperature, the diffusion coefficient in a phase-separated lipid bilayer is always less than in the homogeneous fluid phase. The deviation corresponds to the restriction of lateral diffusion caused by the gel phase, and thus increases markedly when the temperature decreases (higher $1/T$ values) and when the concentration of high-temperature melting component increases (Fig. 3 *A-C*), as both factors increase the proportion of gel phase present in the system. Since the NBD phosphatidylcholine analogs diffuse appreciably only in the liquid crystalline phase, this restriction reports the interactions between the coexisting fluid and the gel phases, and is thus related to the gel phase area fraction and to the gel phase domain topology. The deviations from the fluid-phase values of D are weak in C18C10PC/DSPC (Fig. 3 *A*), more important in C18C10PC/DPPC (Fig. 3 *B*), and increase further in DMPC/DSPC (Fig. 3 *C*). As can be seen from Fig. 2, this progression parallels an increase of the lipid mixture ideality.

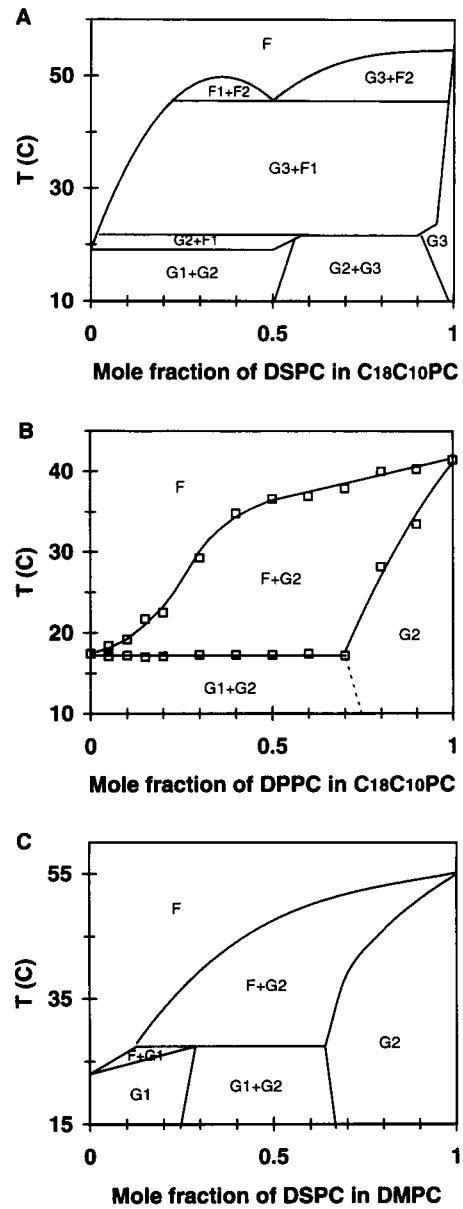

FIGURE 2 Phase diagrams for different phosphatidylcholine mixtures. (*A*) C18C10PC/DSPC (Mason, 1988); (*B*) C18C10PC/DPPC (this study); (*C*) DMPC/DSPC (Knoll et al., 1981); (*F*) fluid; (*G*) gel. The lines in *B* are smooth lines drawn through the onset and completion temperatures (□).

Note that even if their activation energies are similar, the diffusion coefficients in homogeneous fluid phases in Fig. 3, *A* and *B* are much higher than in Fig. 3 *C*. This disagreement addresses the legitimacy of comparing data obtained with a square profile (Vaz et al., 1989, experimental and simulations, this study) and a Gaussian profile (this study, experimental data) of the postbleach fluorophore concentration. Although starting from different initial perturbed states, both methodologies monitor the same phenomenon over similar time and length scales, and we have a priori no reason to believe they should yield different results. The difference in observation radius used in this study (~7 μm

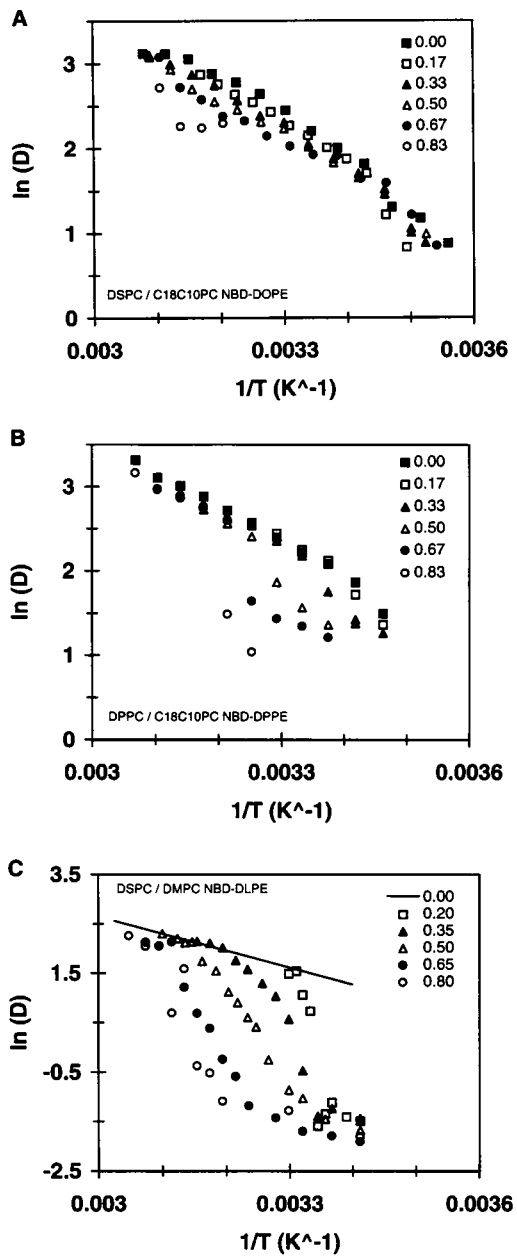

FIGURE 3 Arrhenius plot of the lateral diffusion coefficients. (*A*) C18C10PC/DSPC (this study); (*B*) C18C10PC/DPPC (this study); (*C*) DMPC/DSPC (cooling scans, Vaz et al., 1989). The legends in each plot indicate the molar fraction of the higher temperature melting component. The straight line in *C* represents the diffusion coefficients for the fluid phase, calculated from the data points above the fluidus in DMPC/DSPC (Vaz et al., 1989).

half-width at half-height) and by Vaz et al. (1989) (radius = 3 μm) becomes a critical parameter only if one is to calculate an average size of closed cavities in which the diffusion is restrained above the percolation threshold (Schram et al., 1994). However, it is generally accepted that the diffusion coefficients measured by FRAP do contain an experimental contribution, that can be eliminated by calculating the normalized diffusion coefficient, $D^* = D/D_o$, where D_o stands for the diffusion coefficient of the fluid phase at a given temperature.

D^* values are plotted versus the gel phase area fraction, c, for each lipid mixture in Fig. 4. The gel phase area fraction was calculated from the phase diagrams of Fig. 2, assuming a molecular area of 63 Å^2 for a phosphatidylcholine molecule in the liquid crystalline phase (Lewis and Engelman, 1983) and of 45 Å^2 in the gel phase (Weiner et

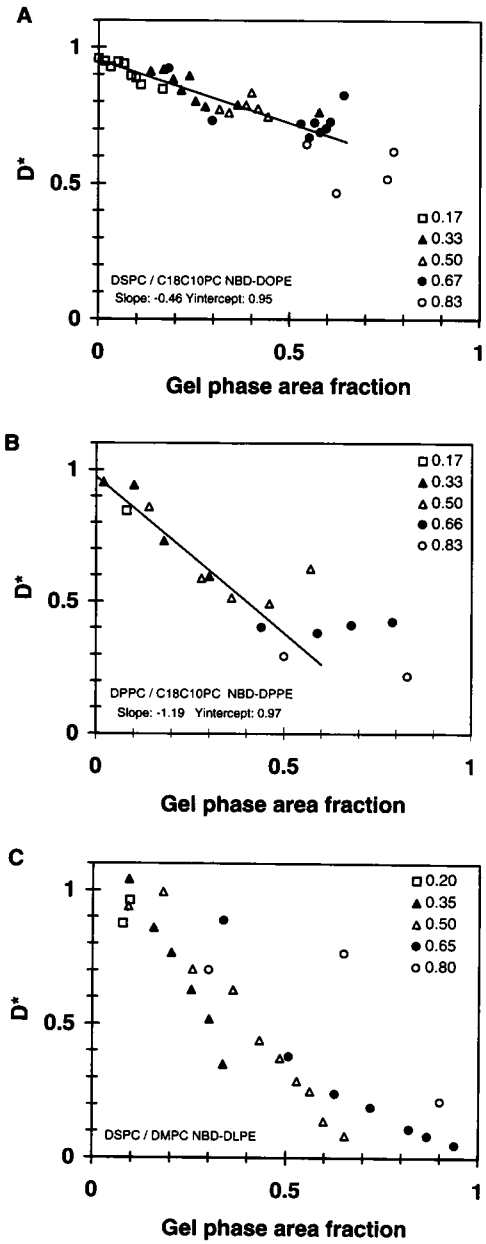

FIGURE 4 Plot of the normalized diffusion coefficients D^* versus the area fraction of gel phase. (*A*) C18C10PC/DSPC (this study); (*B*) C18C10PC/DPPC (this study); (*C*) DMPC/DSPC (Vaz et al., 1989). The legends in each plot indicate the molar fraction of the higher temperature melting component. Straight lines in *A* and *B* are linear regressions, discarding the data points with an associated mobile fraction <0.3 (Fig. 5 *A–B*), slope: −0.46 *y* intercept: 0.95 in *A*, slope: −1.19, *y* intercept: 0.97 in *B*.

al., 1989), independent of acyl-chain length and chain asymmetry. Although not rigorous, these assumptions represent reasonable estimates: the three lipid mixtures display a coexistence region of a liquid crystalline C18C10PC- or DMPC-rich phase and of a gel DPPC- or DSPC-rich phase. Note that the molecular area of C18C10PC was determined by x-ray diffraction to be ~55 Å^2 at 22°C (McIntosh et al., 1984), but because of the lack of resolution of this methodology with fluid lipid bilayers and to the low water content of the sample studied, we did not retain this value. Moreover, introducing 55 Å^2 as the molecular area of fluid C18C10PC barely changes the results in Fig. 4, *A* and *B* and Fig. 5, *A* and *B*.

In C18C10PC/DSPC, D^* decreases regularly and linearly when the gel phase area fraction increases (Fig. 4 *A*). D^* displays a steeper dependence on the gel phase area fraction in the C18C10PC/DPPC mixture, and the data points may still be fitted with a straight line (Fig. 4 *B*). This linear dependence is a good indication that, over the whole range of composition and temperature studied, the topology of the gel phase domains remains almost constant. In contrast, the data of Vaz et al. (1989) obtained in the DMPC/DSPC mixture do not fall on a common plot: if each lipid ratio may be adjusted by a straight line, they all display clearly different trends (Fig. 4 *C*): when the ratio of DSPC to DMPC increases, D^* becomes less dependent on the gel phase area fraction, which unambiguously suggest that the gel phase reorganizes in larger and/or more centrosymmetric domains at high DSPC fraction. Note that the lack of linearity of the data points in Fig. 4 *C* can hardly be accounted for by uncertainties in the diffusion coefficient in the fluid phase: completely unrealistic values of the activation energy are needed to linearize this plot.

This compositional dependence is evidenced in a straightforward way in plots of the mobile fraction versus the gel phase area fraction. If in C18C10PC/DSPC, all the data points fall on a common trendline (Fig. 5 *A*), the mobile fractions exhibit in C18C10PC/DPPC a clear compositional dependence (Fig. 5 *B*) that was not apparent in the normalized diffusion coefficient plot: the higher the fraction of DPPC, the less efficient is the gel phase in compartmentalizing the diffusion plane, which let suppose a reorganization of the gel phase into more compact domains at high concentrations of DPPC. This trend increases further in the DMPC/DSPC mixture, where the compositional dependence is extreme (Fig. 5 *C*). It is noteworthy that for every lipid mixture investigated with either NBD-DOPE (Fig. 5 *A*), NBD-DPPE (Fig. 5 *B*) or NBD-DLPE (Fig. 5 *C*), the M values show an initial plateau region close to 1, meaning that a significant amount of gel phase can exist without any immobilization of the probes. This observation demonstrates that in a two-phase, two-component phosphatidylcholine bilayer investigated by FRAP, the NBD-PE probes report only the diffusion occurring in the liquid crystalline phase, due either to their low solubility in the gel phase, or to a low fluorescence intensity in gel phase subsequent to a modification of the local polarity around the NBD ring

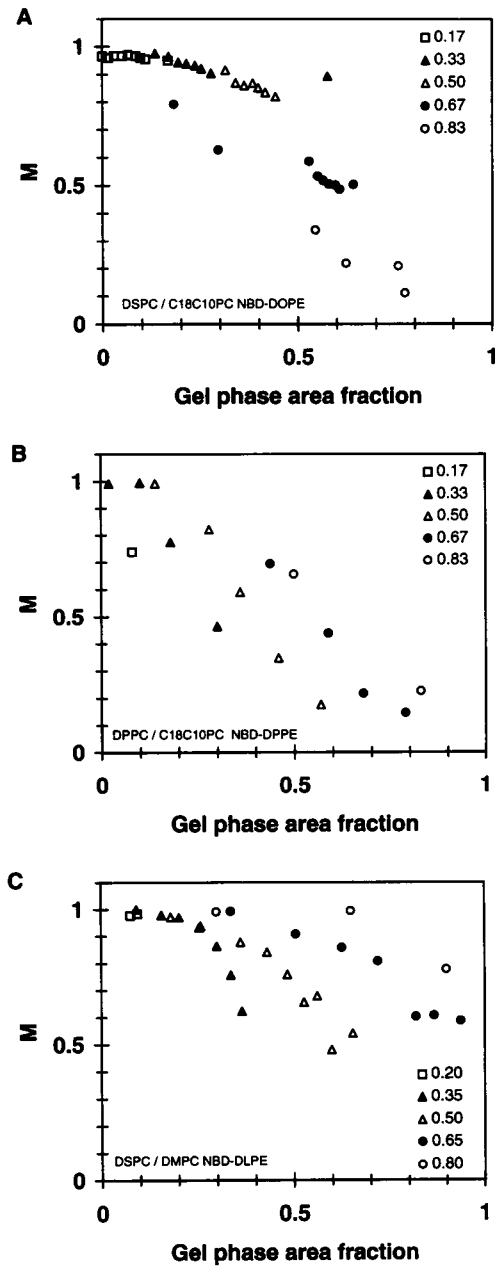

FIGURE 5 Variation of the mobile fraction M versus the area fraction of gel phase. (*A*) C18C10PC/DSPC (this study); (*B*) C18C10PC/DPPC (this study); (*C*) DMPC/DSPC (Vaz et al., 1989). The legends in each plot indicate the molar fraction of the higher temperature melting component.

(Fery-Forgues et al., 1993,) or to auto-quenching resulting from a common exclusion from the gel phase.

Simulations

The normalized diffusion coefficients D^* obtained with randomly distributed point obstacles, and with obstacle aggregates generated with a density of nucleation sites of 1/250 and a probability of aggregation of 1, 1/10, 1/100, and 1/1000 are plotted versus the obstacle area fraction in Fig. 6 *A*. As expected, for randomly distributed point obstacles, D^* decreases

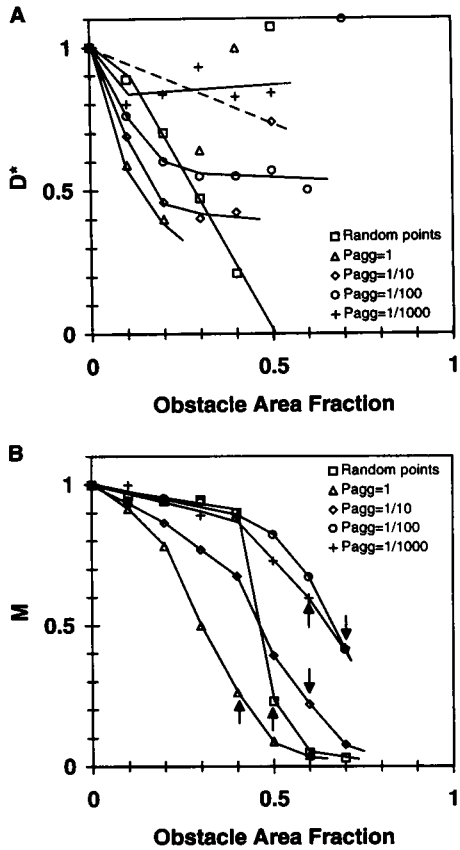

FIGURE 6 Computer-simulated recovery curves. Variation of the normalized diffusion coefficient D^* (*A*) and of the mobile fraction M (*B*) versus the area fraction of obstacles. □, randomly distributed point obstacles. Obstacles aggregates obtained with a density of nucleation sites of 1/250 and a probability of aggregation of △: 1, ◇: 1/10, ○: 1/100 and +: 1/1000. The arrows in *B* correspond to the appearance of a percolating obstacle aggregate (see text). Continuous lines in *A* and *B* are guidelines drawn through the points. Dashed line in *A* is from the Eq. 4 of Schram et al. (1994) for nonoverlapping circles of 250 lattice sites surface.

almost linearly as the obstacle area fraction increases and can be extrapolated at $D^* = 0$ to an obstacle area fraction of 0.5 (Fig. 6 *A*), which is the percolation threshold for a triangular lattice (Saxton, 1989, Stauffer and Aharony, 1992). Above an obstacle area fraction of 0.5, D^* displays an artifactual increase (Table 1) due to the restriction of the diffusion in closed cavities (Schram et al., 1994).

As demonstrated by Saxton (1992), at low obstacle area fraction, obstacle aggregates are more efficient in restricting the diffusion coefficient than randomly distributed point obstacles (Fig. 6 *A*). The higher the probability of aggregation used to generate them, and the more effective they are in decreasing D^*, because of the formation of more extended structures. This tendency is clear at low obstacle area fraction but above $c = 0.2$, D^* increases or exhibits a plateau region (Fig. 6 *A*) well before the matrix is occupied by a percolating obstacle cluster (arrows in Fig. 6 *B*). This behavior comes from an increase of the obstacle aggregate average size, due to aggregates merging, and, to a lesser extent, to an increase of their fractal dimensions with the obstacle area fraction (Table 1). Both factors result in large obstacle aggregates with a slightly more compact structure, that is less effective in obstructing diffusion. Note however that below their respective percolation thresholds, all the relative diffusion coefficients are less than the obstacle-free D^* value (Fig. 6 *A* and Table 1), showing the consistency of the data.

Variations of the mobile fraction versus the obstacle area fraction are reported in Fig. 6 *B*. If for randomly distributed point obstacles, M remains close to 1 up to $c = 0.4$, as little as 20% area fraction of aggregates generated with a probability of aggregation of 1 and 1/10 causes a significant decrease of the mobile fraction (Fig. 6 *B*). A percolating obstacle cluster is formed at $c = 0.4$ for $P_{agg} = 1$, and at $c = 0.6$ for $P_{agg} = 1/10$ (arrows in Fig. 6 *B*; see also Table 1). For lower probabilities of aggregation of 1/100 and 1/1000, M decreases significantly only above $c = 0.4$, and a percolating obstacle aggregate appears at $c = 0.7$ and 0.6, respectively (Table 1).

The key feature in Fig. 6 *B* is that, when the probability of aggregation decreases from 1 to 1/10 to 1/100, there is a systematic shift of the curves toward higher obstacle area fractions, that is a decreasing efficiency in compartmentalizing the diffusion plane. Note that above $c = 0.4$, the obstacle aggregates formed with a probability of aggregation of 1/1000 yield significantly lower mobile fractions than those generated with $P_{agg} = 1/100$. This disagreement is probably due to the large average size and size distribution of the aggregates formed at $P_{agg} = 1/1000$ at high obstacle area fraction (Table 1), which may also account for the relatively broad scattering of the diffusion coefficients obtained with this probability of aggregation (Fig. 6 *A*).

At low obstacle area fraction, the merging of obstacle aggregates during their formation is not frequent and the average aggregate size remains constant around its nominal value, that is 250 lattice sites: $P_{agg} = 1$, 1/10, 1/100, and 1/1000 at an obstacle area fraction of 0.1, and $P_{agg} = 1$, 1/10, and 1/100 at an obstacle area fraction of 0.2 (Table 1). The variation of the relative diffusion coefficient versus the fractal dimension Df of the obstacles obtained at constant average aggregate size is plotted in Fig. 7. Results are compared with what is expected for nonoverlapping circular obstacles (plain two-dimensional objects, that is $Df = 2$) of a surface of 250 sites using the analytical expression of Schram et al. (1994) (Eq. 1). Both models are roughly identical at low obstacle area fractions when the aggregates are well separated from each other. As can be seen from Fig. 7, the values for each obstacle area fraction can be adjusted by a straight line. At 20% obstacle area fraction, there is a monotonic increase of D^* from $P_{agg} = 1$ to 1/10, 1/100, and continuous circles. With 10% obstacle area fraction, the slope is lower, but D^* still increases regularly from $P_{agg} = 1$ to 1/10, 1/100, 1/1000, and continuous circles (Fig. 7).

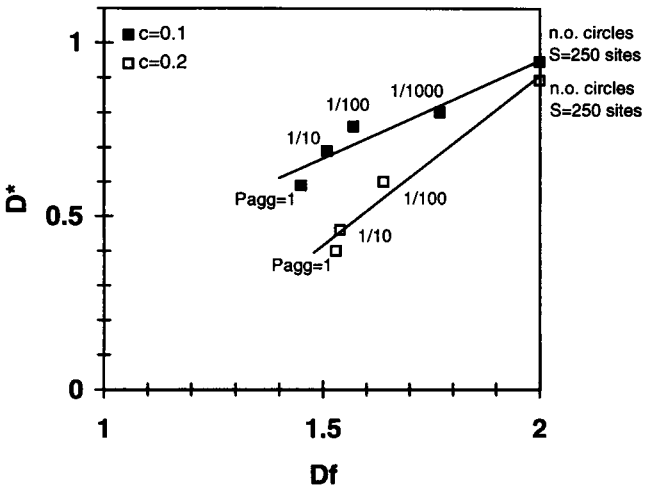

FIGURE 7 Computer simulated recovery curves. Variation of the normalized diffusion coefficient D^* versus the fractal dimension Df of aggregates at constant aggregate average size (~250 sites) for an obstacle area fraction of ■, $c = 0.1$ and □, $c = 0.2$. The values at $Df = 2$ are calculated from Eq. 4 of Schram et al. (1994) for nonoverlapping circles of surface = 250 sites. Straight lines are linear regressions.

DISCUSSION

The lipid mixing properties are probably a key factor regulating the gel phase domain topology: due to a low compositional difference and to a low energetic content of the transition between the coexisting fluid and gel phases, lipid components mixing well together are expected to organize in small and/or ramified gel phase domains and thus to reduce strongly the long-range translational diffusion, whereas immiscible lipids are likely to form large and/or compact gel phase domains, with less influence on the lateral diffusion at comparable gel phase area fractions. The diffusion coefficients obtained in this study on C18C10PC/DSPC and C18C10PC/DPPC mixtures, together with the DMPC/DSPC mixture previously investigated by Vaz et al. (1989), are consistent with this consideration. The increasing efficiency in restricting the diffusion coefficient is particularly clear between C18C10PC/DSPC and both C18C10PC/DPPC and DMPC/DSPC (Fig. 4), and support the view that the gel phase tends to organize in small and/or ramified domains when the ideality of the lipid mixture increases.

Unfortunately, no distinction can be made between a diminution of size and a decrease of the fractal dimension. If a variation of the gel phase domain fractality is expected to have a major effect on the mobile fraction, the compositional dependence of M evidenced in DMPC/DSPC (Fig. 5 *C*) and, to a lesser extent, in C18C10PC/DPPC (Fig. 5 *B*) prevents such an analysis. Nevertheless, this compositional dependence of the mobile fraction is a clear indication that for each of these two lipid mixtures, the gel phase domain topology varies across the phase diagram, as it was previously reported in the literature for DMPC/DSPC: an ESR study of Sankaram et al. (1992) suggests that, in this mixture, the average gel phase domain size increases linearly with the molar fraction of gel phase. This view is further supported by a recent fluorescence quenching investigation that also suggests an increase in the average fluid phase domain size with the proportion of fluid phase in DMPC/DSPC (Piknova et al., 1996). The data in Figs. 4 and 5, however, show a direct correlation between the extent of this compositional dependence and the ideality of the lipid mixture: the higher the miscibility of the lipid compounds, and the more the gel phase domain topology varies.

The decreasing efficiency in compartmentalizing the diffusion plane when the proportion of high-temperature melting component increases (Fig. 5, *B* and *C*) can be accounted for by considering a variation of the gel phase domain shape rather than size. To obtain a quantitative estimate of the influence of the obstacle fractality on the mobile fraction and diffusion coefficient measured by FRAP, we have developed simple computer simulations of fluorescence recovery curves in a matrix obstructed with aggregates of point obstacles. A diffusion-limited aggregation process, described in Material and Methods, was used to generate randomly distributed obstacles of various fractal dimensions with an average size of 250 sites (lipid molecules). That is the order of magnitude expected for a gel phase domain in a phase-separated two-component phosphatidylcholine bilayer (Almeida et al., 1992, Sankaram et al., 1992). Note that because of cluster merging during their formation, the average aggregate size increases rapidly above an obstacle area fraction of 0.2 (Table 1).

We do not mean to suggest that this diffusion-limited aggregation model is the actual mechanism involved at a molecular level in the lateral phase separation process. We, therefore, do not relate the probability of aggregation between point obstacles to a lipid mixing nonideality parameter (von Dreele, 1978). However, this model might be representative of the lateral phase separation if one assumes that phase separation proceeds via the initial formation of circular gel phase domains of small size that diffuse and aggregate at a later stage, as suggested by Florsheimer and Mohwald (1989). The model may also be applied to the aggregation process of a trans-membrane protein. One site of the lattice would then correspond either to a small-size gel phase domain or to a protein molecule, but provided that the aggregate junctions are tight and obstruct the translational diffusion of the fluid-phase lipid molecule, this rescaling of the matrix should not affect the results if the diffusion coefficients are renormalized.

In the present study, we adopt the point of view that the model generates obstacle aggregates whose size and fractality have the same impact on the diffusion coefficient and mobile fraction measured by the FRAP as the actual gel phase domains. The detailed mechanism used to generate the aggregates should not have an influence on the way their size and fractality obstruct the lateral diffusion. Two major conclusions can be drawn from these simulations:

1) At low obstacle area fraction, where the average aggregate size remains constant around 250 lattice sites, the

relative diffusion coefficient increases linearly with the fractality of the aggregates, with a slope increasing with c (Fig. 7). This relation, valid only in an essentially open diffusion plane (mobile fraction close to 1), does not depend on the observation area and thus may be generalized to experimental FRAP data if the average size of the gel phase domains can be deduced from other approaches, such as ESR (Sankaram et al., 1992).

2) As expected, the efficiency in compartmentalizing the diffusion plane, i.e., in decreasing the mobile fraction, depends strongly on the obstacle fractality. At constant average aggregate size (that is for $c \leq 0.2$ in Fig. 6 *B*), highly extended obstacles are much more efficient to do so than compact ones (Fig. 6 *B*). When considering the aggregate merging, the variation of M with a decreasing probability of aggregation deduced from the simulations (Fig. 6 *B*) closely resembles the compositional dependence evidenced in the mobile fractions by DMPC/DSPC (Fig. 5 *C*) and, to a lesser extent, C18C10PC/DPPC (Fig. 5 *B*), and thus strongly suggests that the fractal dimension of the gel phase domain increases with the proportion of high temperature melting component in DMPC/DSPC and (slightly) in C18C10PC/DPPC.

Because the diffusion coefficients in C18C10PC/DPPC display no clear compositional dependence (Fig. 4 *B*), the increase of the gel phase domain fractal dimension with the proportion of DPPC has to be compensated by a reduction of their size to keep D at an almost constant value. In DMPC/DSPC, the reorganization of the gel phase domains into more compact structures at high proportions of DSPC seen on the mobile fractions (Fig. 5 *C*) is consistently reflected by a reduced efficiency to restrict the diffusion coefficient (Fig. 4 *C*), but the linear increase of the gel phase domain size with the gel phase area fraction deduced by ESR in DMPC/DSPC by Sankaram et al. (1992) might have been overestimated. These authors did not consider a variation of the domain shape, which may be crucial in terms of spin-spin interactions. We could not deduce from the FRAP data obtained on DMPC/DSPC nor on C18C10PC/DPPC a consistent trend between either D or M and the gel phase area fraction. Besides the differences in the dynamics sampled by the ESR spectroscopy and the FRAP, it could be that the fraction of the coexisting fluid and gel phases as well as their composition are both involved in determining gel phase domains topology.

In the C18C10PC/DSPC mixture, both the diffusion coefficients and the mobile fractions fall on common trendlines (Figs. 4 *A* and 5 *A*): the results obtained for this highly immiscible mixture may thus be analyzed in terms of nonoverlapping circular obstacles of identical size. Using the phenomenological equation of Schram et al. (1994):

$$D^* = 1 - [1.574 - 0.475 \cdot \ln(r)] \cdot c \qquad (1)$$

where r is the obstacle radius expressed in (triangular) l.s. Considering that below a mobile fraction of 0.3, the recoveries are too small to be meaningful in the time window used, and discarding the corresponding points, we obtained a size for the gel phase domains of ~500 lipid molecules in C18C10PC/DSPC, which is probably a good estimate of their actual size. This value was determined from a simple linear regression of the data points in Fig. 4 *A* with an associated mobile fraction of more than 0.3, to take into account possible uncertainties in the diffusion coefficient in the all-fluid phase. The y-intercept is, however, very close to 1, showing the consistency of the data. Not surprisingly, a similar approach on C18C10PC/DPPC yields an obstacle size of ~20 lipid molecules (Fig. 4 *B*), too small to be the actual size of the gel phase domains.

Due to the interplay of the obstacle size and fractality, which may compensate for each other, the FRAP data obtained on DMPC/DSPC and C18C10PC/DPPC mixtures cannot be analyzed further. However, the variation of the gel phase domain fractality with the global lipid composition seen in DMPC/DSPC and C18C10PC/DPPC, combined with other investigations pointing to a variation across the phase diagram of the size of the gel and fluid phase domains in DMPC/DSPC (Piknova et al., 1996, Sankaram et al., 1992), suggests that the lateral organization adopted by a phase-separated two-component lipid bilayer becomes more dependent, in terms of size and fractality, of the proportion of the coexisting fluid and gel phase but also of their composition, when the ideality of the mixture increases. Dynamic local heterogeneities, which are likely to increase with the mixture ideality, probably further complicate the lateral organization. These considerations may be especially relevant in terms of membrane microdomain formation, since variation of either the global lipid composition or of the lipid acyl chains seems to promote drastic changes in the long-range membrane topology.

REFERENCES

Abney, J. R., B. A. Scalettar, and J. C. Owicki. 1989. Self diffusion of interacting membrane proteins. *Biophys. J.* 55:817–833.

Almeida, P. F. F., W. L. C. Vaz, and T. E. Thompson. 1992. Lateral diffusion and percolation in two-phase, two-component lipid bilayers. Topology of the solid-phase domains in-plane and across the lipid bilayer. *Biochemistry.* 31:7198–7210.

Barros, F., A. Naoumi, M. L. Viriot, and J. C. Andre. 1991. Lateral diffusion in synthetic membranes: models and experiments on protein influence. *J. Chem. Soc. Far. Trans.* 87:2039–2046.

Bultmann, T., W. L. C. Vaz, E. C. C. Melo, R. B. Sisk, and T. E. Thompson. 1991. Fluid-phase connectivity and translational diffusion in a eutectic, two-component, two-phase phosphatidylcholine bilayer. *Biochemistry.* 30:5573–5579.

Eisinger, J., J. Flores, and W. P. Petersen. 1986. A milling crowd model for local and long-range obstructed lateral diffusion. *Biophys. J.* 49: 987–1001.

Fery-Forgues, S., J. P. Fayet, and A. Lopez. 1993. Drastic changes in the fluorescence properties of NBD probes with the polarity of the medium: involvement of a TITC state. *J. Photochem. Photobiol. A.* 70:229–243.

Florsheimer, M., and H. Mohwald. 1989. Development of equilibrium domain shapes in phospholipid monolayers. *Chem. Phys. Lipids.* 49: 231–241.

Halladay, H. N., R. E. Stark, S. Ali, and R. Bittman. 1990. Magic-angle spinning NMR studies of molecular organization in multibilayers formed by 1-octadecanoyl-2-decanoyl-*sn*-glycero-3-phosphocholine. *Biophys. J.* 58:1449–1461.

Hui, S. W., J. T. Mason, and C. Huang. 1984. Acyl chain interdigitation in saturated mixed-chain phosphatidylcholine bilayer dispersions. *Biochemistry.* 23:5570–5577.

Jorgensen, K., M. M. Sperotto, O. G. Mouritsen, J. H. Ipsen, and M. J. Zuckermann. 1993. Phase equilibria and local structure in binary lipid bilayers. *Biochim. Biophys. Acta.* 1152:135–145.

Jorgensen, K., and O. G. Mouritsen. 1995. Phase separation dynamics and lateral organization of two-component lipid membrane. *Biophys. J.* 95:942–954.

Knoll, W., K. Ibel, and E. Sackmann. 1981. Small-angle neutron scattering study of lipid phase diagrams by the contrast variation method. *Biochemistry.* 20:6379–6383.

Koppel, D. E. 1979. Fluorescence redistribution after photobleaching. A new multipoint analysis of membrane translational dynamics. *Biophys. J.* 28:281–292.

Lewis, B. A., and D. M. Engelman. 1983. Lipid bilayer thickness varies linearly with acyl chain length in fluid phosphatidylcholine vesicles. *J. Mol. Biol.* 166:211–217.

Lopez, A., L. Dupou, A. Altibelli, J. Trotard, and J. F. Tocanne. 1988. Fluorescence recovery after photobleaching (FRAP) experiments under conditions of uniform disk illumination. *Biophys. J.* 53:963–970.

McIntosh, T. J., S. A. Simon, J. C. Ellington, and N. A. Porter. 1984. New structural model for mixed-chain phosphatidylcholine bilayers. *Biochemistry.* 23:4038–4044.

Mason, J. T. 1988. Mixing behavior of symmetric chain length and mixed chain length phosphatidylcholines in two-component multilamellar bilayers: evidence for gel and liquid-crystalline phase immiscibility. *Biochemistry.* 27:4421–4429.

Mason, J. T. 1994. Properties of phosphatidylcholine bilayers as revealed by mixed-acyl phospholipid fluorescent probes containing n-(9-anthroyloxy) fatty acids. *Biochim. Biophys. Acta.* 1194:99–108.

Piknova, B., D. Marsh, and T. E. Thompson. 1996. Fluorescence quenching study of percolation and compartmentalization in two-phase lipid bilayer. *Biophys. J.* 71:892–897.

Sankaram, M. B., D. Marsh, and T. E. Thompson. 1992. Determination of fluid and gel domain sizes in two-component, two phase lipid bilayers. *Biophys. J.* 63:340–349.

Saxton, M. J. 1989. Lateral diffusion in an archipelago: distance dependence of the diffusion coefficient. *Biophys. J.* 56:615–622.

Saxton, M. J. 1992. Lateral diffusion and aggregation: a Monte Carlo study. *Biophys. J.* 61:119–128.

Sheetz, M. P., M. Schindler, and D. E. Koppel. 1980. Lateral mobility of integral membrane proteins is increased in spherocytic erythrocytes. *Nature.* 285:510–512.

Schram, V., J. F. Tocanne, and A. Lopez. 1994. Influence of obstacles on lipid lateral diffusion: computer simulation of FRAP experiments and application to proteoliposomes and biomembranes. *Eur. Biophys. J.* 23:337–348.

Schram, V., and T. E. Thompson. 1995. Interdigitation does not affect translational diffusion of lipids in liquid crystalline bilayers. *Biophys. J.* 69:2517–2520

Slater, J. L., and C. Huang. 1988. Interdigitated bilayer membranes. *Prog. Lipids Res.* 27:325–359.

Stauffer, D., and A. Aharony. 1992. Introduction to Percolation Theory. Taylor and Francis, London.

Tocanne, J. F. 1992. Detection of lipid domains in biological membranes. *Comm. Mol. Cell. Biophys.* 8:53–72.

Vaz, W. L. C., F. Goodsaid-Zalduondo, and K. Jacobson. 1984. Lateral diffusion of lipids and proteins in bilayer membranes. *FEBS Lett.* 174: 199–207.

Vaz, W. L. C., R. M. Clegg, and D. Hallmann. 1985. Translational diffusion of lipids in liquid crystalline phase phosphatidylcholine multilayers. A comparison of experiment with theory. *Biochemistry.* 24: 781–786.

Vaz, W. L. C. Translational diffusion in phase-separated lipid bilayer membranes. 1992. *Comm. Mol. Cell. Biophys.* 8:17–36.

Vaz, W. L. C., E. C. C. Melo, and T. E. Thompson. 1989. Translational diffusion and fluid domain connectivity in a two-component, two-phase phospholipid bilayer. *Biophys. J.* 56:869–876.

Vaz, W. L. C., E. C. C. Melo, and T. E. Thompson. 1990. Fluid phase connectivity in an isomorphous, two-component, two-phase phosphatidylcholine bilayer. *Biophys. J.* 58:273–275.

von, Dreele P. H. 1978. Estimation of lateral species separation from phase transitions in non-ideal two-dimensional lipid mixtures. *Biochemistry.* 17:3939–3943.

Weiner, M. C., M. R. Suter, and J. F. Nagle. 1989. Structure of the fully hydrated gel phase of dipalmitoyl phosphatidylcholine. *Biophys. J.* 55: 315–325.

Wolf, D. E., V. M. Maynard, C. A. McKinnon, and D. L. Melchior. 1990. Lipid domains in the rat sperm plasma membrane demonstrated by differential scanning calorimetry. *Proc. Natl. Acad. Sci. USA.* 87: 6893–6896.